Automated wind velocity profiling from adaptive optics telemetry

Douglas J. Laidlaw,[1,2]★ James Osborn,[1] Timothy J. Morris,[1] Alastair G. Basden,[1]
Eric Gendron,[3] Gérard Rousset,[3] Matthew J. Townson,[1] and Richard W. Wilson[1]
[1] *Centre for Advanced Instrumentation (CfAI), Durham University, South Road, Durham, DH1 3LE, United Kingdom.*
[2] *German Aerospace Center (DLR), Institute of Communications and Navigation, 82234, Weßling, Germany.*
[3] *LESIA, Observatoire de Paris, Université PSL, CNRS, Sorbonne Université, Univ. Paris Diderot, Sorbonne Paris Cité, 5 place Jules Janssen, 92195 Meudon, France.*

Accepted XXX. Received YYY; in original form ZZZ

ABSTRACT

Ground-based adaptive optics (AO) systems can use temporal control techniques to greatly improve image resolution. A measure of wind velocity as a function of altitude is needed to minimize the temporal errors associated with these systems. Spatio-temporal analysis of AO telemetry can express the wind velocity profile using the SLODAR technique. However, the limited altitude-resolution of current AO systems makes it difficult to disentangle the movement of independent layers. It is therefore a challenge to create an algorithm that can recover the wind velocity profile through SLODAR data analysis. In this study we introduce a novel technique for automated wind velocity profiling from AO telemetry. Simulated and on-sky centroid data from CANARY - an AO testbed on the 4.2 m William Herschel telescope, La Palma - is used to demonstrate the proficiency of the technique. Wind velocity profiles measured on-sky are compared to contemporaneous measurements from Stereo-SCIDAR, a dedicated high-resolution atmospheric profiler. They are also compared to European centre for medium-range weather forecasts. The software package that we developed to complete this study is open source.

Key words: turbulence - atmospheric effects - instrumentation: adaptive optics - telescopes

1 INTRODUCTION

The angular resolution of ground-based optical telescopes is primarily limited by atmospheric refractive index fluctuations. Adaptive optics (AO) systems on ground-based telescopes commonly utilize Shack-Hartmann wavefront sensors (SHWFSs) to measure phase aberrations across an observed wavefront. The AO system can then work to correct the wavefront by actuating a number of deformable mirrors (DMs). Multi-conjugate AO (MCAO) and multi-object AO (MOAO) systems can achieve high angular resolution in wide-field astronomy by tomographically reconstructing the wavefront across a large field of view (FOV). To optimize wavefront correction these systems need to know how the optical turbulence strength varies with altitude (Tallon, Foy & Vernin 1992; Neichel, Fusco & Conan 2009). Wavefront correction must be updated in real-time because the wind is continuously moving turbulent cells across the light-path of the telescope. To reduce temporal errors, predictive control algorithms can help mitigate the latency between the measurement of a wavefront and its successive DM correction. These algorithms commonly require optical turbulence and wind velocity profile information (Jackson et al. 2015). Accurate wind velocity profile information has been shown to significantly improve the performance of these controllers (Sivo et al. 2014). It is also believed that by measuring the wind velocity profile, the altitude-resolution of the optical turbulence profile can be improved (Wang et al. 2008). Additionally, wind velocity information can be used to study the Taylor frozen-flow hypothesis (Taylor G. I. 1938; Schöck & Spillar 2000; Guesalaga et al. 2014).

Slope detection and ranging (SLODAR; Wilson 2002) is a widely used technique for optical turbulence profiling. It triangulates the vertical structure of the optical turbulence profile by calculating the cross-covariance between SHWFS centroids from independent guide stars (GSs). The SLODAR technique requires SHWFS information and can therefore be used in tandem with certain AO systems. Averaging non-orthogonal centroid cross-covariance as a function of baseline represents the optical turbulence profile in what is known as a covariance map. The optical turbulence profile, SHWFS

★ E-mail: douglas.laidlaw@dlr.de

misalignments and vibration artifacts can be recovered by fitting an analytical model to the measured covariance map. It is common practice for SLODAR data analysis to utilize the covariance map (Butterley, Wilson & Sarazin 2006; Cortés et al. 2012; Guesalaga et al. 2014; Ono et al. 2016). More recently, it has been shown that analytically fitting to a covariance map region of interest (ROI) optimizes the accuracy and efficiency of the SLODAR technique (Laidlaw et al. 2018).

Calculating the cross-covariance between temporally offset SHWFS centroid measurements demonstrates the wind velocity profile. In the covariance map, this temporal offset disjoints the optical turbulence profile. Each shift within the temporally offset covariance map corresponds to the velocity of a specific turbulent layer. It has been shown that the wind velocity profile can be recovered by peak tracking individual turbulent layers within a spatio-temporal cross-covariance array (Osborn et al. 2017; Sivo et al. 2018). However, the number of SHWFS sub-apertures can cause an AO system to have a limited altitude-resolution. Having a limited altitude-resolution results in wind velocity profile information becoming quickly entangled as individual layers can travel in various directions with different speeds. This makes it difficult to write an algorithm for automated peak tracking.

This study introduces a novel technique for automated wind velocity profiling from AO telemetry. It makes use of a recommended AO parameter estimation technique (Laidlaw et al. 2018). This technique measures the optical turbulence profile, SHWFS misalignments and vibration artifacts. Once parameter estimation is complete, a temporally offset covariance map can be fitted to by each analytically generated layer running its altitude and baseline position as a free parameter. If frozen-flow is assumed the change in covariance map location for each layer is synonymous with its velocity. A qualitative study of the wind velocity profiling technique is carried out using simulated natural guide star (NGS) and laser guide star (LGS) data from CANARY, an AO demonstrator for Extreme Large Telescope (ELT) technologies on the 4.2 m William Herschel telescope (WHT), La Palma. We also demonstrate our wind velocity profiling technique using on-sky CANARY data (Morris et al. 2014). On-sky wind speed profiling results are compared to European centre for medium-range weather forecasts (ECMWF). They are also compared to contemporaneous profiles that were measured using the scintillation detection and ranging (SCIDAR; Shepherd et al. 2013) technique. These profiles were measured by the Stereo-SCIDAR instrument that was being operated on the 2.5 m Isaac Newton telescope (INT), La Palma (Osborn et al. 2015). The INT is roughly 400 m east of the WHT.

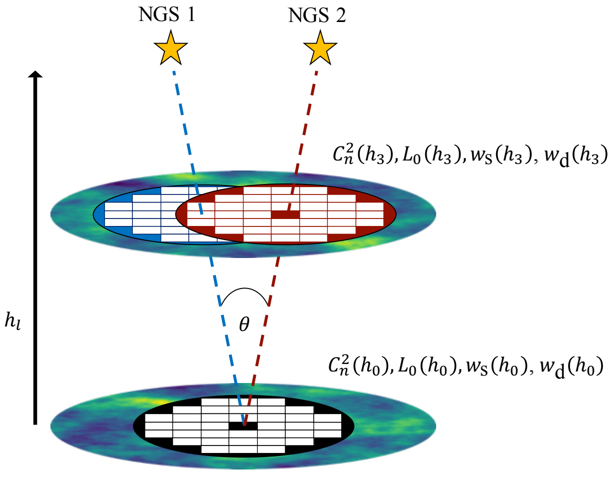

Figure 1. Sub-aperture optical paths of two 7 × 7 SHWFSs to NGS 1 (black→blue) and NGS 2 (black→red). The two turbulent layers are at altitudes of 0 and $3D/7\theta$ km.

2 MEASURING THE OPTICAL TURBULENCE PROFILE

To measure the vertical structure of the optical turbulence profile the SLODAR technique requires at least two SHWFSs that are measuring the optical phase of sufficiently luminous GSs. For two optically aligned SHWFSs the altitude of NGS sub-aperture optical path intersection, h_l, is given by

$$h_l = \frac{l s_{\mathrm{w}}}{\theta}. \tag{1}$$

The distance between the centers of two adjacent sub-apertures and the angular separation between the NGSs are denoted s_{w} and θ, respectively. l represents the sub-aperture separation order, i.e. the number of sub-apertures by which meta-pupil SHWFSs are separated. Fig. 1 shows a 2-NGS system monitoring an optical turbulence profile of $N_{\mathrm{L}} = 2$, where N_{L} denotes the number of layers. These two layers are at altitudes h_0 and h_3. If D is the diameter of the telescope then the maximum altitude of sub-aperture optical path intersection, $h_{\max}$, is $(D - s_{\mathrm{w}})/\theta$. The SLODAR technique is applicable to all asterisms but it should be noted that equation 1 is only valid for NGS position angles of 0, 90, 180 and 270°.

It has been shown that the SLODAR technique is applicable to LGSs (Cortés et al. 2012). However, the altitude of LGS sub-aperture optical path intersection, a_l, is

$$a_l = \frac{n l s_{\mathrm{w}}}{\theta n + l s_{\mathrm{w}}}. \tag{2}$$

$a_l \leq h_l$ because of the cone effect. In equation 2, n is the distance to each LGS and it is assumed that n is the same for all LGSs.

The spatio-temporal macroscopic phase of each layer can be broken down into four constituents: refractive index structure function, outer scale, speed and direction. These are given by $C_n^2(h)$, $L_0(h)$, $w_{\mathrm{s}}(h)$ and $w_{\mathrm{d}}(h)$, respectively.

2.1 Covariance map

The SLODAR technique requires open-loop or pseudo open-loop SHWFS centroids. Orthogonal centroid measurements are made by each SHWFS sub-aperture as the wind blows turbulent layers across the light-path of the telescope. Measurements from NGS 1 and NGS 2 are written x_1, y_1 and x_2, y_2, respectively. The cross-covariance is then calculated between each combination of independent SHWFS centroids that are measured along non-orthogonal axes, e.g. cov(x_1,x_2)

Table 1. Simulated system parameters in the Soapy configuration file.

System parameter	Value
NGS apparent magnitude	10
Telescope diameter	4.2 m
Air mass	1
Monochromatic wavelength	500 nm
Frame rate	150 Hz
Number of frames	10,000
Throughput	0.3
Read-out noise	1 electron per pixel

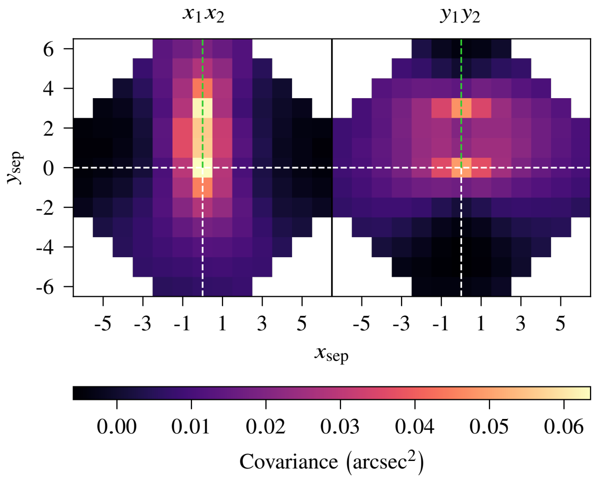

Figure 2. Covariance map from simulated SHWFS centroids for the $N_{\rm L} = 2$ configuration shown in Fig. 1. Both layers have $r_0 = 0.1$ m and $L_0 = 25$ m. Dashed lines have been overlaid to indicate $x_{\rm sep}, y_{\rm sep} = (0, 0)$ (white) and the GS position angle, γ (green).

and cov(y_1,y_2) for the configuration shown in Fig. 1. Each SHWFS combination then averages cross-covariance as a function of sub-aperture separation in x and y ($x_{\rm sep}$ and $y_{\rm sep}$, respectively). The resultant array is known as a covariance map.

A 2-NGS 7 × 7 SHWFS covariance map is shown in Fig. 2. The covariance map in Fig. 2 corresponds to Fig. 1, i.e. there is a turbulent layer at 0 and $3D/7\theta$ km. Both layers are characterized by $L_0 = 25$ m and $r_0 = 0.1$ m, where r_0 denotes the Fried parameter. The SHWFS centroids used to calculate Fig. 2 were simulated using Soapy[1]: a Monte Carlo AO simulation package (Reeves 2016). Table 1 lists the values used in the Soapy configuration file. For this type of system it is believed that 10,000 frames optimizes its statistical convergence (Martin 2014).

The position angle of the NGSs in the FOV of the telescope is given by γ. For a multi-GS system, the covariance map from each GS combination is calculated. All of these covariance maps are then stacked into a single array that is referred to as M_0.

2.2 Covariance parameterization of optical turbulence and SHWFS misalignments

We have developed an algorithm for analytically generating the covariance between sub-apertures. The full mathematical description for analytically generating sub-aperture covariance has been outlined previously (Martin et al. 2016). The analytical covariance for each turbulent layer depends on r_0, L_0, h, sub-aperture separation and optical alignment. By controlling these inputs we can generate a covariance map array that allows us to iteratively fit an analytical model to SHWFS cross-covariance measurements. Multiple NGS or LGS combinations can be fitted to simultaneously. The fitting technique we use is referred to as covariance parameterization of optical turbulence and SHWFS misalignments (CAPT; Laidlaw et al. 2018). CAPT was written to be an AO system supervisor that can be implemented on any telescope. The CAPT software package is open source[2].

3 MEASURING THE WIND VELOCITY PROFILE

3.1 Temporally offset covariance map

Calculating the cross-covariance between temporally offset SHWFS centroid measurements causes each turbulent layer to be independently shifted away from its M_0 origin. This can be visualized by studying h_3 in Fig. 1. If Taylor frozen-flow is assumed and the SHWFS observing NGS 2 has its centroids temporally offset, this corresponds to the phase observed by the red meta-pupil being shifted with the movement of the turbulent layer. In covariance-space this translates to the turbulent layer being linearly displaced from its M_0 origin. Each turbulent layer has its own displacement vector. The angle of the displacement vector is the direction in which the turbulent layer is passing across the light-path of the telescope. For the example above, the angle of the h_3 displacement vector is $w_{\rm d}(h_3)$. The magnitude of its change in baseline location is $\omega w_{\rm s}(h_3)/f$, where f is the frame rate and ω is the number of frames that have been offset.

We stack the negatively temporal offset covariance map alongside its positive reciprocal. This is to help conserve $w_{\rm d}(h)$ and to prevent wind velocity profile information from becoming entangled. If displacement vectors are large enough turbulent layers can be moved off the edge of a temporally offset covariance map. The inclusion of both positive and negative temporal offsets helps prevent this from resulting in the loss of wind velocity profile information. Fig. 3 shows a covariance map that has been calculated from temporally offset centroid measurements. A single layer has been simulated at the ground with $r_0 = 0.1$ m, $L_0 = 25$ m and $w_{\rm d} = 37°$. The centroids were simulated using Soapy and the system was parameterized by the values listed in Table 1. The negatively temporal offset covariance map is highlighted by having its values multiplied by -1. In an optically aligned system the ground-layer is centered in M_0 at $x_{\rm sep}, y_{\rm sep} = (0,0)$, i.e. where the dashed lines are centered in Fig. 2 and Fig. 3. It can be seen in Fig. 3 that after introducing a temporal offset the ground-layer has been shifted

---

[1] https://github.com/AOtools/soapy

[2] https://github.com/douglas-laidlaw/capt

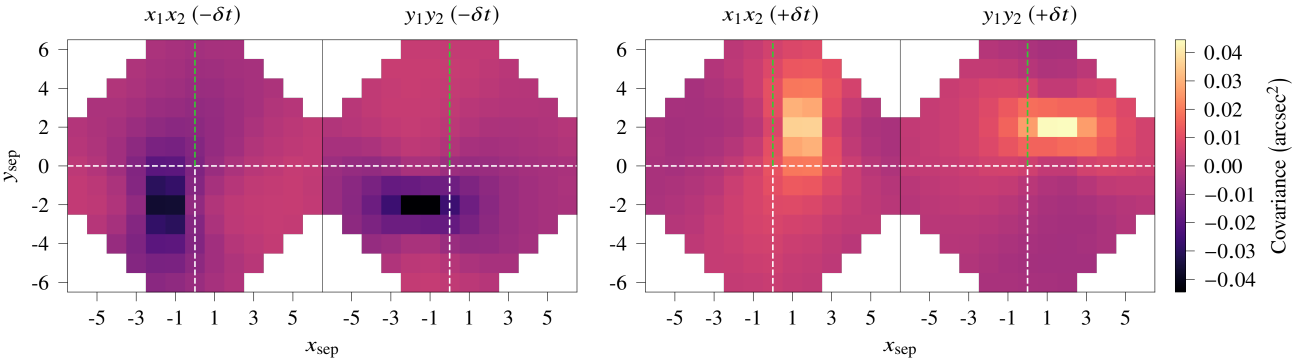

Figure 3. Temporally offset covariance map from simulated SHWFS centroids for $N_{\mathrm{L}} = 1$ at 0 km. The layer is characterized by $r_0 = 0.1$ m and $L_0 = 25$ m. Dashed lines have been overlaid to indicate $x_{\mathrm{sep}}, y_{\mathrm{sep}} = (0, 0)$ (white) and the GS position angle, γ (green).

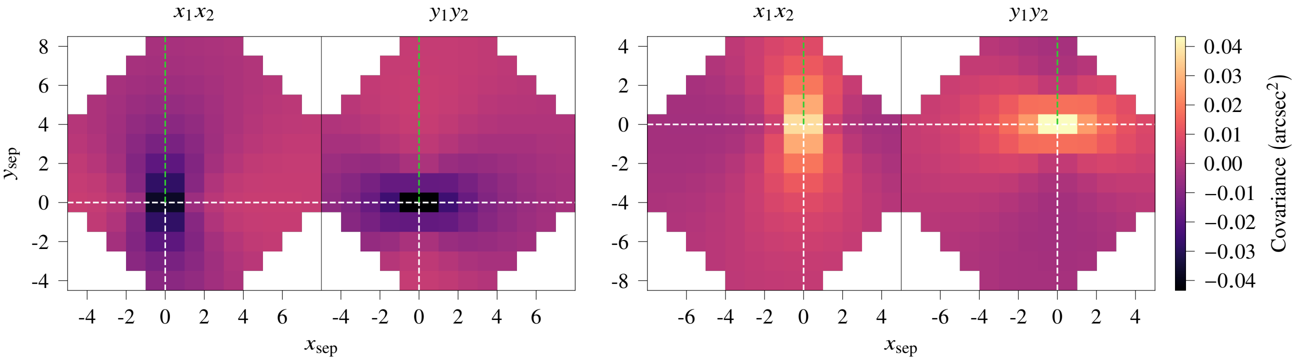

Figure 4. The LMA fit to Fig. 3. The analytically generated layer was fitted to Fig. 3 by the measured ground-layer from CAPT iteratively adjusting h, x_{sep} and y_{sep}. Dashed lines have been overlaid to indicate $x_{\mathrm{sep}}, y_{\mathrm{sep}} = (0, 0)$ (white) and the GS position angle, γ (green).

away from this location. The measured temporally offset covariance map array is referred to as $M_{\delta t}$, where δt denotes the temporal offset ω/f.

3.2 Subtracting ground-layer isoplanatic turbulence

It is well-documented that turbulence statistics for the ground-layer deviate from the Kolmogorov model (Lehtonen, Correia & Helin 2018). This is largely attributed to ground-layer measurements being influenced by turbulence within the dome of the telescope (Guesalaga et al. 2014). If the ground-layer has non-Kolmogorov statistics then its cross-covariance function will differ from the analytical model. This prevents accurate measurements of turbulent layers at non-zero altitudes. However, it is possible to mitigate the ground-layer but subtracting ground-layer isoplanatic turbulence. To perform this subtraction, the mean centroid for each sub-aperture location is calculated at every frame. All centroids from every SHWFS then have their respective mean centroid subtracted, i.e. each sub-aperture location has common-motion removed. Subtracting ground-layer isoplanatic turbulence also removes vibration artifacts. This common-motion removal can be replicated in the model used for generating analytical sub-aperture covariance (Martin et al. 2016; Laidlaw et al. 2018). By subtracting ground-layer isoplanatic turbulence the analytical model can therefore independently study turbulent layers at non-zero altitudes.

3.3 Covariance parametrization of wind velocity

The key to spatio-temporal wind velocity profiling is being able to track turbulent layers from M_0 to $M_{\delta t}$. In this section we present a novel technique for wind velocity profiling that uses the Levenberg-Marquardt algorithm (LMA) to iteratively fit an analytical model to temporally offset SHWFS cross-covariance measurements. Multiple NGS or LGS combinations can be fitted to simultaneously. The user decides how many layers to fit and at which altitudes. The model we use for analytically generating sub-aperture covariance is the same that is used by CAPT. We refer to this wind velocity profiling technique as covariance parametrization of wind velocity (CAW). The 3 steps of CAW are as follows:

1. Use CAPT to measure the optical turbulence profile along with SHWFS misalignments and vibration artifacts (Laidlaw et al. 2018).

2. The temporally offset covariance map array is calculated for SHWFS centroids with subtracted ground-layer isoplanatic turbulence. LMA takes $C_n^2(h > 0)$, $L_0(h > 0)$ and

SHWFS misalignments from 1, and fits the wind velocity profile at non-zero altitudes by each analytically generated layer running h, x_{sep} and y_{sep} as a free parameter. The positive and negative temporally offset covariance map arrays are fitted to simultaneously, i.e. the negative temporal offset is fitted to by analytically generating layers with the same parameters but at all values of h, $-x_{\mathrm{sep}}$ and $-y_{\mathrm{sep}}$.

3. Wind velocity profile information from 2 is used in conjunction with parameter estimation from 1 to analytically generate a covariance map array that dissociates the ground-layer from $M_{\delta t}$. The LMA then takes SHWFS misalignments, vibration artifacts, $C_n^2(0)$ and $L_0(0)$ from 1, and fits to ground-layer $M_{\delta t}$ by having the analytically generated ground-layer run h, x_{sep} and y_{sep} as free parameters. As in 2, the positive and negative temporally offset covariance map arrays are fitted to simultaneously.

CAW was written to run alongside CAPT and is also open source[3]. To operate CAW the user must know the physical parameters of the system, e.g. the dimensions of its SHWFSs. These parameters are imported by CAW using a configuration file that is provided with its open source software. The CAW fitting parameters, e.g. the size of the temporal offset, are set in a separate configuration file that is also provided. To analyze SHWFS centroid measurements CAW requires the position of the GSs as well as the air mass of the observation. All of the open source algorithms are written in Python using the NumPy (van der Walt et al. 2011) and SciPy (Jones et al.) libraries. Example test cases are included in the open source package.

Each of the measured altitudes from the first step of CAW (CAW 1) are the integrated turbulence strength across an altitude range. Within this altitude range $w_{\mathrm{s}}(h)$ and $w_{\mathrm{d}}(h)$ will not necessarily be constant. This means that the wind velocity profile in $M_{\delta t}$ might not primarily originate from the altitudes set in CAW 1. This is why h needs to be fitted in conjunction with x_{sep} and y_{sep} during the second and third step of CAW (CAW 2 and CAW 3, respectively). The $C_n^2(h)dh$ noise-floor in CAW 1 is $10^{-16}\,\mathrm{m}^{1/3}$. Only $C_n^2(h)$ values greater than the noise-floor are fitted during CAW 2 and CAW 3. The main difference between CAW and peak tracking (outlined in Section 1) is that peak tracking is trying to best-fit specific values within $M_{\delta t}$. CAW is utilizing the ability to analytically generate covariance to find the least-squares minimum of the entire temporally offset covariance map array, i.e. every data point within $M_{\delta t}$ contributes to the detection of a wind velocity measurement. It can be imagined that Fig. 3 is the ground-only $M_{\delta t}$ that is fitted to during CAW 3. The analytical fit to Fig. 3 is shown in Fig. 4. It is important to note the difference in axes between Fig. 3 and Fig. 4. We denote the change in x_{sep} and y_{sep} for each turbulent layer as $\Delta x_{\mathrm{sep}}(h)$ and $\Delta y_{\mathrm{sep}}(h)$. The wind speed profile is therefore given by

$$w_{\mathrm{s}}(h) = \frac{\sqrt{\Delta x_{\mathrm{sep}}(h)^2 + \Delta y_{\mathrm{sep}}(h)^2}}{\delta t}. \tag{3}$$

The wind direction profile can be calculated from the magnitudes of $\Delta x_{\mathrm{sep}}(h)$ and $\Delta y_{\mathrm{sep}}(h)$.

3.4 Validating wind velocity measurements

While operating CAW it is unrealistic to assume that the analytical model will perfectly match SHWFS cross-covariance measurements. There are a number of reasons for this, e.g. the turbulence being non-Kolmogorov. As the LMA is performing a two-dimensional least-squares fit, there must be a system in place to validate wind velocity profiling detections. The presented solution runs CAW twice: once at the studied temporal offset, ω/f, and once at $(\omega-1)/f$. The wind velocity measurements from ω/f and $(\omega-1)/f$ temporal offsets are given the superscript m and v, respectively, i.e. $w_{\mathrm{s}}^{\mathrm{m}}(h^{\mathrm{m}})$ is validated by $w_{\mathrm{s}}^{\mathrm{v}}(h^{\mathrm{v}})$. A wind velocity measurement is deemed false if any of the following conditions are satisfied:

1. $|w_{\mathrm{s}}^{\mathrm{m}}(h^{\mathrm{m}}) - w_{\mathrm{s}}^{\mathrm{v}}(h^{\mathrm{v}})| > 5\,\mathrm{m/s}$
2. $|w_{\mathrm{d}}^{\mathrm{m}}(h^{\mathrm{m}}) - w_{\mathrm{d}}^{\mathrm{v}}(h^{\mathrm{v}})| > 30°$
3. $|h^{\mathrm{m}} - h^{\mathrm{v}}| > h_{\mathrm{max}}/10$
4. $h^{\mathrm{m}} > h_{\mathrm{max}}$ or $h^{\mathrm{v}} > h_{\mathrm{max}}$.
5. $w_{\mathrm{s}}^{\mathrm{m}}(h^{\mathrm{m}}) > 100\,\mathrm{m/s}$ or $w_{\mathrm{s}}^{\mathrm{v}}(h^{\mathrm{v}}) > 100\,\mathrm{m/s}$.
6. The location of the turbulent layer is not within $M_{\delta t}$.

The values chosen to satisfy 1 to 4 were selected through testing CAW in simulation. Condition 5 is included as 100 m/s is the upper limit of the expected atmospheric wind speed. For the values listed an incorrect detection would always satisfy multiple conditions. It should also be noted that this validation technique is independent of AO system parameters, e.g. the number of SHWFS sub-apertures.

4 RESULTS

4.1 Wind velocity profiling from simulated AO telemetry

Open-loop NGS SHWFS centroids were simulated for a 4-NGS CANARY configuration in Soapy. Each SHWFS had 7 × 7 sub-apertures. The median results within the European southern observatory documentation (ESO; ESO 2015) were used to parameterize the simulated 35-layer optical turbulence and wind speed profile. The 35-layer ESO profile does not include wind direction. The simulated wind direction profile followed an example radiosonde measurement (Hirsch, Agassi & Koren 2011). The outer scale of every simulated layer was 25 m and integrated r_0 was 0.1 m. The 4-NGS system had a square layout with $h_{\mathrm{max}} = 24\,\mathrm{km}$. The values in the Soapy configuration file were the same as those listed in Table 1. The simulation was repeated 10 times.

The CAW fitting procedure was performed on the simulated SHWFS centroids. The six 7×7 SHWFS combinations were fitted to simultaneously using 7 evenly-spaced layers from 0 to 24 km. As they were not included in the simulation, vibration artifacts and SHWFS misalignments were found to be negligible. The optical turbulence profiling results from CAW 1 are shown in Fig. 5. We use the mean deviation, F_{md}, to quantify the optical turbulence profiling results (Laidlaw et al. 2018), where

$$F_{\mathrm{md}} = \frac{1}{N_{\mathrm{L}}}\sum_{i=1}^{N_{\mathrm{L}}}\left|\log_{10}\left(C_n^2(h_i)^{\mathrm{m}} \big/ C_n^2(h_i)^{\mathrm{r}}\right)\right|. \tag{4}$$

Equation 4 is the average order of magnitude difference between the measured and reference $C_n^2(h)$ profiles ($C_n^2(h)^{\mathrm{m}}$

---

[3] https://github.com/douglas-laidlaw/caw

Table 2. Simulated ESO 35-layer profile compared to the NGS and LGS results from Fig. 5.

	F_{md}	D	A_{rms} (m/s)	B (m/s)
NGS	0.11 ± 0.02	0.80 ± 0.02	2.2 ± 0.3	0.2 ± 0.2
LGS	0.06 ± 0.01	0.75 ± 0.04	2.0 ± 0.1	1.1 ± 0.2

Table 3. Simulated ESO 35-layer profile compared to the NGS and LGS results from Fig. 6.

	F_{md}	D	A_{rms} (m/s)	B (m/s)
NGS	0.08 ± 0.01	0.40 ± 0.08	2.7 ± 0.7	0.5 ± 0.4
LGS	0.04 ± 0.01	0.33 ± 0.05	1.9 ± 0.5	−1.4 ± 0.3

and $C_n^2(h)^{\mathrm{r}}$, respectively). The altitudes where turbulence strength is fitted are denoted by their layer number, i. $C_n^2(h)^{\mathrm{r}}$ is calculated by integrating the 35-layer ESO profile across the evenly-spaced fitted altitudes, i.e. if the bins have an altitude width b_{w}, at altitude h_i the input profile is integrated between $h_i - b_{\mathrm{w}}/2$ and $h_i + b_{\mathrm{w}}/2$.

The wind velocity results are also shown in Fig. 5. For reasons discussed in Section 4.2, CAW was operated with $\omega = 8$. However, the simulation results were similar for all appropriate ω values. The reason for this is that the 35 layers were simulated with frozen-flow. The wind velocity profile was fitted for all 7 layers because each layer was measured above the noise-floor. Out of the 10 simulations, the layers fitted at 20 and 24 km were validated (see Section 3.4) 6 and 0 times, respectively. This is why only 6 measured layers are shown for the NGS wind profiling results in Fig. 5. A number of factors are attributed to this: the layers that failed to be validated are the weakest and therefore carry the least weight during CAW 2; they are positioned towards the edge of the covariance map where the SNR is relatively low; they are slow-moving and therefore their measured cross-covariance function might not have converged to match the analytical model. The number of validated wind velocity profile candidates divided by the total number of candidates is denoted D. The layers that have been validated closely follow the trend of the simulated wind speed and direction profiles. The relatively large errors at 21 km are thought to originate from CAW fitting near h_{max}.

The root mean squared deviation, A_{rms}, and bias, B, are used to quantify the accuracy of $w_{\mathrm{s}}^{\mathrm{m}}(h^{\mathrm{m}})$, where

$$A_{\mathrm{rms}} = \sqrt{\frac{1}{DN_{\mathrm{L}}}\sum_{i=1}^{DN_{\mathrm{L}}}\left(w_{\mathrm{s}}^{\mathrm{m}}(h_i^{\mathrm{m}}) - w_{\mathrm{s}}^{\mathrm{r}}(h_i^{\mathrm{r}})\right)^2}, \tag{5}$$

$$B = \frac{1}{DN_{\mathrm{L}}}\sum_{i=1}^{DN_{\mathrm{L}}}\left(w_{\mathrm{s}}^{\mathrm{m}}(h_i^{\mathrm{m}}) - w_{\mathrm{s}}^{\mathrm{r}}(h_i^{\mathrm{r}})\right). \tag{6}$$

In Equations 5 and 6, the superscript r denotes the reference altitude and wind speed. $w_{\mathrm{s}}^{\mathrm{r}}(h^{\mathrm{r}})$ is the reference wind speed at altitudes h^{r}, where each value of h_i^{r} is the nearest neighbor to h_i^{m}. As $w_{\mathrm{d}}^{\mathrm{m}}(h^{\mathrm{m}})$ is given in polar coordinates, it is not possible to quantify the accuracy of $w_{\mathrm{d}}^{\mathrm{m}}(h^{\mathrm{m}})$ for all wind directions. The CAW results from the NGS simulated dataset are summarized in Table 2.

The NGS study was repeated for sodium LGSs that had an apparent magnitude of 8 and were focussed at an altitude of 90 km. The SHWFSs were simulated to measure a monochromatic wavelength of 589 nm. All of the other simulated parameters were the same as those listed in Table 1. Due to the cone effect the maximum altitude of sub-aperture optical path intersection for the LGS asterism was roughly 19 km. Therefore, when repeating the CAW 1 measurement on the simulated dataset a layer was not fitted at 24 km. The LGS optical turbulence profiling results are shown in Fig 5. As the fitted layer at 20 km has its bin extend past the maximum altitude of sub-aperture optical path intersection, it is not included in LGS F_{md} analysis. The 6 layers fitted in CAW 1 were fitted during CAW 2 and CAW 3. Out of the 10 simulations, the layers fitted at 16 and 20 km were validated 6 and 0 times, respectively. The mean validated layers are shown alongside the NGS results in Fig. 5. The CAW results from the LGS simulated dataset are summarized in Table 2. LGS F_{md} is less than NGS F_{md}. However, if the NGS optical turbulence profile only considers layers from 0 to 16 km then NGS $F_{\mathrm{md}} = 0.03$.

As mentioned in Section 3.3, the wind velocity across an altitude range will not necessarily be constant. We refer to this process as wind shear and it is frequently observed on-sky (Osborn et al. 2017). It is therefore important to understand the detrimental effects of wind shear when using CAW to study the wind velocity profile. To do this we repeated the NGS and LGS simulations, but with a wind direction profile that had exaggerated wind shear. By analyzing a non-naturalistic wind velocity profile, we were able to test the robustness of CAW. The simulated profile and its corresponding results are shown in Fig. 6. The results from Fig. 6 are summarized in Table 3. In Fig. 6 the measured $C_n^2(h)$ profile is different than in Fig.5. This is attributed to the wind velocity profile biasing results. For example, the layers near 2 and 24 km are moving in the same direction at roughly the same speed. This will be influencing turbulence profile values in the measured covariance map array.

The accuracy of CAW is reduced when studying a profile with non-naturalistic wind shear. It is unable to validate the majority of its measurements. However, the majority of its validated measurements closely follow the simulated wind velocity profile. For the NGS results the largest deviation occurs at roughly 16 km, where CAW measures its wind speed to be over twice the reference wind speed. The largest deviation for the LGS results also occurs at roughly 16 km, where the wind direction measurement from CAW is less than the reference wind direction by almost 25°. Fitting more layers with a narrower bin width would reduce the effects of wind shear. This requires SHWFSs with more sub-apertures and so it is expected that the effects of wind shear will be reduced when applying CAW to larger-scale AO systems.

4.2 Wind velocity profiling from on-sky AO telemetry

In this section we demonstrate the operation of CAW for on-sky data. The analyzed datasets were recorded using the CANARY instrument that was being operated on the 4.2 m WHT. The MOAO capabilities of CANARY have been previously demonstrated (Gendron et al. 2014; Vidal et al. 2014; Martin et al. 2017). Each dataset was in a 4-NGS con-

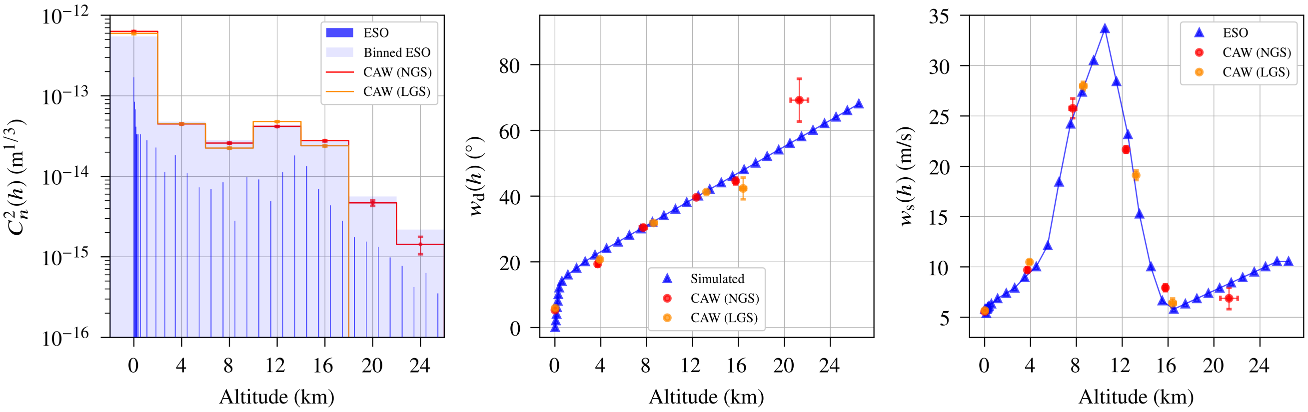

Figure 5. Optical turbulence and wind velocity profiling results when using CAW to study simulated data from a realistic profile. Shown are the optical turbulence (left), wind direction (middle) and the wind speed (right) profiling results.

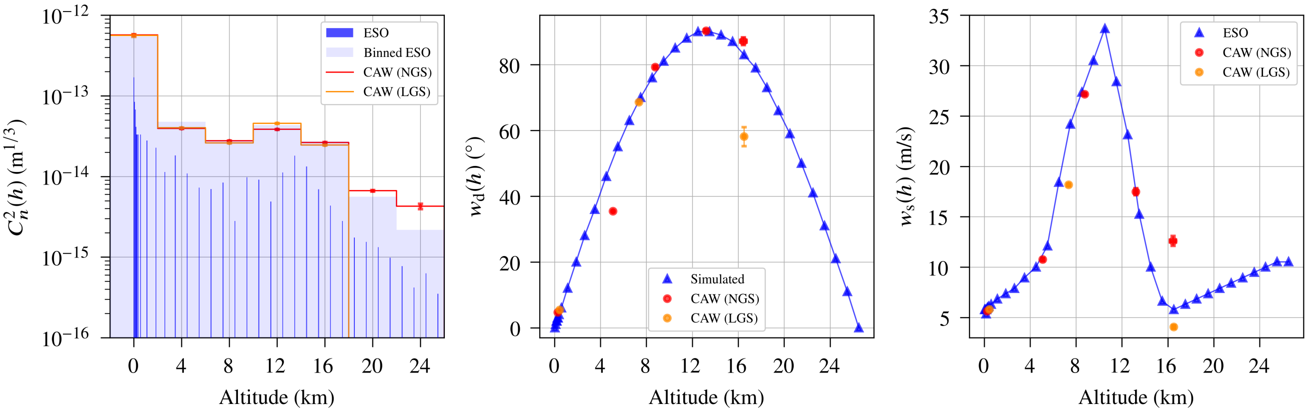

Figure 6. Optical turbulence and wind velocity profiling results when using CAW to study simulated data from a profile that has non-naturalistic wind shear. Shown are the optical turbulence (left), wind direction (middle) and the wind speed (right) profiling results.

figuration and each NGS was monitored by an independent 7×7 SHWFS. Within every dataset each SHWFS recorded 10,000 open-loop centroid measurements at a frame rate of approximately 150 Hz. LGSs are not considered during this section because there were not enough open-loop LGS datasets. The results from CANARY were compared to contemporaneous measurements from the Stereo-SCIDAR instrument. Stereo-SCIDAR was being operated on the 2.5 m INT. The time interval between a measurement from Stereo-SCIDAR and CANARY centroid-data retrieval was limited to 20 minutes. It was assumed that both the optical turbulence and wind velocity profile would not drastically alter within this timescale. In total there were 27 useful datasets. These observations were made in July and October of 2014. Although all datasets could be used to compare optical turbulence profile measurements, Stereo-SCIDAR post-processing had filtered out the wind velocity measurements from 4, i.e. only 23 wind velocity datasets could be compared between CANARY and Stereo-SCIDAR. However, we were able to compare all 27 measurements to the ECMWF.

CAW 1 was performed on the CANARY dataset, fitting 7 evenly-spaced layers between 0 and 24 km. No layer above $h_{\max}$ was fitted. For each dataset the six 7×7 SHWFS combinations were fitted to simultaneously. The Stereo-SCIDAR $C_n^2(h)$ profiles were binned to the resolution of CAW 1 to give $C_n^2(h)^{\mathrm{r}}$ (the same binning process as outlined in Section 4.1). The noise-floor of $C_n^2(h)^{\mathrm{r}} dh$ was 10^{-16} m$^{1/3}$. To be included in F_{md} analysis, each fitted layer in $C_n^2(h)^{\mathrm{m}}$ was required to be below $h_{\max}$ and within the maximum altitude bin of Stereo-SCIDAR. The $C_n^2(h)$ log-log plot between CANARY and Stereo-SCIDAR is shown in Fig. 7.

CAW 2 and CAW 3 were performed on the CANARY dataset. Wind velocity profiling was carried out for $\omega = 1$ to 30 (the wind velocity profile measurement at $\omega = 1$ was used to validate the measurement at $\omega = 2$). The comparisons to Stereo-SCIDAR and ECMWF showed a minimum A_{rms} at $\omega = 8$. The high A_{rms} results at small values of ω implied that the turbulent layers needed a larger temporal offset to disentangle from γ. The most likely reason for the A_{rms} increase at $\omega > 8$ is the fragmentation of the frozen-flow approximation, i.e. the turbulent phase of each layer has started to decay from its fixed state. Frozen-flow fragmentation might vary with $C_n^2(h)$ and $w_{\mathrm{s}}(h)$. However, $\omega = 8$ is found to be the best-fit average. For CANARY, $\omega = 8$ corresponds to roughly 0.05 s.

The wind speed scatter plots for CANARY versus

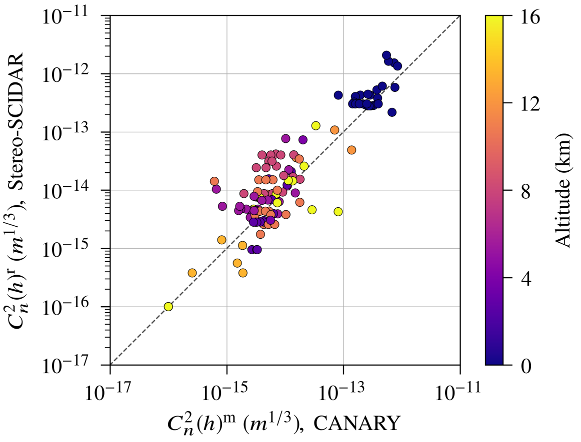

Figure 7. Log-log plot of binned Stereo-SCIDAR and CANARY optical turbulence profile measurements from CAW 1 (CAPT). The black dashed line plots $C_n^2(h)^{\mathrm{m}} = C_n^2(h)^{\mathrm{r}}$.

Table 4. Comparing CAW results from on-sky CANARY data to Stereo-SCIDAR and the ECMWF. The CAW results were obtained by fitting to spatio-temporal covariance maps with $\omega = 8$.

	Stereo-SCIDAR	ECMWF
F_{md}	0.38 ± 0.04	-
D	0.85 ± 0.03	0.84 ± 0.03
A_{rms} (m/s)	3.5 ± 0.3	4.0 ± 0.3
B (m/s)	-0.2 ± 0.4	-0.7 ± 0.3

Stereo-SCIDAR and CANARY versus ECMWF are shown in Fig. 8 and Fig. 9, respectively. The results shown in Fig. 7, Fig. 8 and Fig. 9 are summarized in Table 4. Showing the wind direction scatter plots would be unrepresentative as wind direction is measured in polar coordinates. Discrepancies between the measurements in Fig. 7 and Fig. 8 can be attributed to the INT and WHT both having unique dome and local environmental seeing conditions; the telescopes not observing the same direction; and the data from the telescopes not being retrieved at the exact same instant. The results from Stereo-SCIDAR and the ECMWF will also be influenced by their own sources of error. Our wind speed comparisons also use nearest neighbor measurements. This means that the wind speed measurements we are comparing were not all recorded at the exact same altitude. Furthermore, as shown in Section 4.1, wind shear might be causing erroneous results. To decrease wind shear errors the AO system must be able to measure more layers with a narrower bin width, e.g. the effects of wind shear will be significantly reduced when applying CAW to an ELT-scale AO system.

5 CONCLUSIONS

We have presented a novel technique for automated wind velocity profiling from AO telemetry. This enables AO system control techniques that significantly improve image resolution. The introduced wind velocity profiling technique is referred to as CAW. We tested CAW using simulated data from CANARY. The simulated optical turbulence and wind speed profiles were parameterized with the 35-layer ESO profile. For the NGS simulation, the wind speed bias and root mean squared deviation were measured to be $B = 0.2 \pm 0.2$ m/s and $A_{\mathrm{rms}} = 2.2 \pm 0.3$ m/s, respectively. CAW was also shown to be equally applicable to LGS analysis. An additional set of simulations explored what happens when CAW fits to layers that are experiencing wind shear. We saw that wind shear can cause erroneous results. However, under wind shear the majority of the measurements from CAW were still accurate and we measured $B = 0.5 \pm 0.4$ m/s and $A_{\mathrm{rms}} = 2.7 \pm 0.7$ m/s.

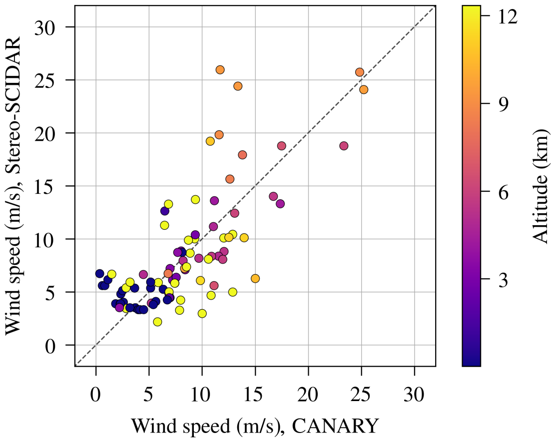

Figure 8. Stereo-SCIDAR versus the CANARY results from using CAW with $\omega = 8$. Measurements from Stereo-SCIDAR are taken as the nearest neighbors to h^{m}. The black dashed line plots $w_{\mathrm{s}}^{\mathrm{m}}(h^{\mathrm{m}}) = w_{\mathrm{s}}^{\mathrm{r}}(h^{\mathrm{r}})$.

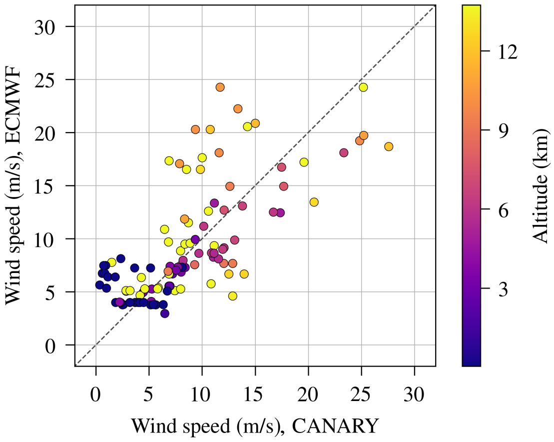

Figure 9. ECMWF versus the CANARY results from using CAW with $\omega = 8$. Measurements from ECMWF are taken as the nearest neighbors to h^{m}. The black dashed line plots $w_{\mathrm{s}}^{\mathrm{m}}(h^{\mathrm{m}}) = w_{\mathrm{s}}^{\mathrm{r}}(h^{\mathrm{r}})$.

On-sky CANARY wind speed profiling results from CAW were compared against wind speed profiles from Stereo-SCIDAR and the ECMWF. In both comparisons A_{rms} was minimized when $\omega = 8$. This minimum suggested that, on average, 0.05 s is the optimal temporal offset for frozen-flow to describe the wind velocity profile. When compared to Stereo-SCIDAR: $A_{\mathrm{rms}} = 3.5 \pm 0.3$ m/s and $B = -0.2 \pm 0.4$ m/s. When compared to the ECMWF: $A_{\rm rms} = 4.0 \pm 0.3$ m/s and $B = -0.7 \pm 0.3$ m/s.

CAW is an accurate and reliable AO telemetry wind velocity profiling technique. It bypasses challenges that peak tracking is unable to overcome. This is an important development for the data processing tools that are to be built for forthcoming ELT era instruments.

ACKNOWLEDGEMENTS

All of the plots were rendered in Matplotlib (Hunter 2007). The William Herschel Telescope and the Isaac Newton Telescope are operated on the island of La Palma by the Isaac Newton Group in the Spanish Observatorio del Roque de los Muchachos of the Instituto de Astrofísica de Canarias. The work carried out at both of these telescopes was supported by the Science and Technology Funding Council, UK (grant CG ST/P000541/1) and the European Commission (FP7 Infrastructures OPTICON grant 226604, 312430, and H2020 grant 730890). We thank the UK Programme for the European Extremely Large Telescope (ST/N002660/1) for supporting this research. We would also like to thank the reviewer of this publication for their constructive comments.

REFERENCES

Butterley T., Wilson R. W., Sarazin M., 2006, MNRAS, 369, 835-845

Cortés A., Neichel B., Guesalaga A., Osborn J., Rigaut F., Duzman D., 2012, MNRAS, 427, 2089-2099

Gendron E., Vidal F., Brangier M., Morris T., Hubert Z., Basden A., Rousset G., Myers R., Chemla F., Longmore A., Butterley T., Dipper N., Dunlop C., Geng D., Gratadour D., Henry D., Laporte P., Looker N., Perret D., Sevin A., Talbot G., Younger E., 2011, Astronomy & Astrophysics, 529

Guesalaga A., Neichel B., Cortes A., Béchet C., Guzmán D., 2014, MNRAS, 440, 1925-1933

Hirsch E., Agassi E., Koren I., 2011, AMT, Vol. 4, No. 1, 117-130

Hunter J. D., Matplotlib: A 2D graphics environment, Computing In Science & Engineering, Vol. 9, 90-95, 2007

Jackson K., Correia C., Lardière O., Andersen D., Bradley C., 2015, OSA, Vol. 40, Issue 2, 143-146

Jones E., Oliphant T., Peterson P, and Others, SciPy: Open source scientific tools for Python

Laidlaw D., Osborn J., Morris T., Basden A., Beltramo-Martin O., Butterley T., Gendron E., Reeves A., Rousset G., Townson M., Wilson R., 2018, MNRAS, 483, 4341-4353

Lehtonen J., Correia C. M., Helin T., 2018, SPIE Proceedings, Adaptive Optics Systems VI, 10703

Martin O., 2014, Université Paris-Diderot, Démonstration sur le ciel de l′optique adaptative multi-objet avec étoiles lasers par CANARY

Martin O., Correia C. M., Gendron E., Rousset G., Vidal F., Morris T. J., Basden A. G., Myers R. M., Ono Y. H., Neichel B., Fusco T., 2016, SPIE, Adaptive Optics Systems V, 9909

Martin O. A., Gendron E., Rousset G., Gratadour D., Vidal F., Morris T. J., Basden A. G., Myers R. M., Correia C. M., Henry D., 2017, Astronomy & Astrophysics, 598

Morris T., Gendron E., Basden A., Martin O., Osborn J., Henry D., Hubert Z., Sivo G., Gratadour D., Chemla F., Sevin A., Cohen M., Younger E., Vidal F., Wilson R., Butterley T., Bitenc U., Reeves A., Bharmal N., Raynaud H., Kulcsar C., Conan J., Huet J., Perret D., Dickson C., Atkinson D., Baillie T., Longmore A., Todd S., Talbot G., Morris S., Rousset G., Myers R., 2014, SPIE Proceedings, Adaptive Optics Systems IV, 8447

Neichel B., Fusco T., Conan J-M., 2009, OSA, Vol. 26, Issue 1, 219-235

Ono Y. H., Correia C. M., Andersen D. R., Lardière O., Oya S., Akiyama M., Jackson K., Bradley C., 2016, MNRAS, 465, 4931

Osborn J., Butterley T., Perera S., Fohring D., Wilson R. W., 2015, Journal of Physics: Conference Series, 595, 012022

Osborn J., Butterley T., Townson M., Reeves A. P., Morris T. J., Wilson R. W., 2017, MNRAS, 464, 3998

Reeves A., 2016, SPIE Proceedings, Adaptive Optics Systems V, 9909

Relevant Atmospheric Parameters for E-ELT AO Analysis and Simulations, ESO-258292, Version 2

Schöck M., Spillar E. J., 2000, OSA, Vol. 17, Issue 9, 1650-1658

Sivo G., Kulcsár C., Conan J-M., Raynaud H-F., Gendron E., Basden A., Vidal F., Morris T., Meimon S., Petit C., Gratadour D., Martin O., Hubert Z., Sevin A., Perret D., Chemla F., Rousset G., Dipper N., Talbot G., Younger E., Myers R., Henry D., Todd S., Atkinson D., Dickson C., Longmore A., 2014, OSA, Issue 19, 23565-23591

Sivo G., Turchi A., Masciadri E., Guesalaga A., Neichel B., 2018, MNRAS, 476, 999-1009

Shepherd H. W., Osborn J., Wilson R., Butterley T., Avila R., Dhillon V. S., Morris T., 2013, MNRAS, 437, 3568-3577

M. Tallon, R. Foy, and J. Vernin., 1992, 3-D Wavefront Sensing for Multiconjugate Adaptive Optics. 42, 517

Taylor G. I., 1938, RSP, Vol. 164, No. 919, 476-490

van der Walt S., Chris Colbert S., Gaël, V., The NumPy array: a structure for efficient numerical computation, Computing in Science & Engineering, Vol. 13, 22-30, 2011

Vidal F., Gendron É., Rousset G., Morris T., Basden A., Myers R., Brangier M., Chemla F., Dipper N., Gratadour D., Henry D., Hubert Z., Longmore A., Martin O., Talbot G., Younger E., 2014, Astronomy & Astrophysics, 569

Wang L., Schöck. Chanan G., 2008, Vol. 47, Issue 11, 1880-1892

Wilson R., 2002, MNRAS, 337, 103-108

This paper has been typeset from a TEX/LATEX file prepared by the author.